ACS APPLIED MATERIALS & INTERFACES

Interfacial Engineering to Tailor the Properties of Multifunctional Ultralight Weight hBN-Polymer Composite Aerogels

Sehmus Ozden, Nikita S. Dutta, Katelyn Randazzo, Thierry Tsafack, Craig B. Arnold,* and Rodney D. Priestley*

Cite This: *ACS Appl. Mater. Interfaces* 2021, 13, 13620−13628

Read Online

ACCESS | Metrics & More | Article Recommendations | SI Supporting Information

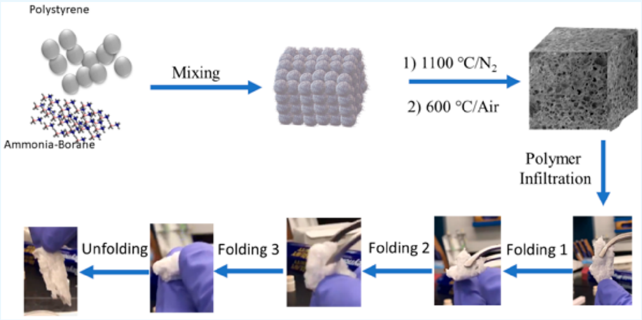

ABSTRACT: A common feature of aerogels is that they are brittle and suffer from poor mechanical properties. The development of high-performance, lightweight, and mechanically robust polymer composite aerogels may find use in a broad range of applications such as packaging, transportation, construction, electronics, and aerospace. Most aerogels are made of ceramic materials, such as silica, alumina, and carbide. These aerogels are dense and brittle. Two-dimensional (2D) layered nanostructures such as graphene, graphene oxide and hexagonal boron nitride (hBN) have promising potential in emerging technologies including those involved in extreme environmental conditions because they can withstand high temperatures, harsh chemical environments, and corrosion. Here, we report the development of highly porous, ultralightweight, and flexible aerogel composites made by the infiltration of various polymers into 2D hBN aerogels. The 2D hBN aerogels in which pore size could be controlled were fabricated using a unique self-assembly approach involving polystyrene nanoparticles as templates for ammonia borane into desired structures. We have shown that the physical, mechanical, and thermal properties of hBN-polymer composite aerogels can be tuned by the infiltration of different additives. We also performed theoretical calculations to gain insight into the interfacial interactions between the hBN-polymer structure, as the interface is critical in determining key material properties.

KEYWORDS: *aerogels, multifunctional composites, interface engineering, energy dissipation, fire resistant*

INTRODUCTION

Aerogels are porous solids with many attractive attributes, such as low density, heat conduction, high porosity, surface area, and fire resistance.[1−3] The development of low density and mechanically robust fire-resistant aerogels with control over physical, mechanical, and thermal properties is of scientific interest due to their potential commercial impact in a broad range of applications such as packaging, transportation, construction, electronics, telecommunications, energy conversion, storage materials, sensors, and aerospace.[4−9] Currently, aerogel technologies face many challenges including cost-effective production and material durability. Underlying the manufacturing challenges is the critical need for greater control of assembly of the molecular building blocks that form aerogels, which would provide a method to tune final porous arrangement, orientation, and molecular interactions. Control of the manufacturing process offers a great opportunity to overcome challenges of tuning the density, mechanical, and thermal properties of aerogels.

To date, various strategies have been developed, such as freeze-casting, chemical cross-linking, and chemical vapor deposition (CVD) growth for fabricating innovative aerogels with the desired characteristics of low density, thermal conductivity, good mechanical durability, chemical inertness, and high porosity.[9−11] Various aerogels made from silica, metal (e.g., copper oxide and silver aerogels), polymer (e.g., polyimide and cellulose aerogels), and carbon have been fabricated.[5,6,10,12−16] The properties of these aerogels are usually affected by the intrinsic properties of the solid components, such as density and cellular architectures. For developing an appropriate assembly that can sustain structural integrity upon large mechanical deformation, various material compositions with different architectures have been reported.[17,18]

Recently, 2D-layered material-based aerogels have been developed.[17−21] The higher dimensionality as compared to 0D and 1D nanostructures gives 2D material-based aerogels a distinct advantage for developing ultralightweight, mechanically robust, and fire-resistant hierarchical aerogels.[11,19]

Received: September 18, 2020
Accepted: February 18, 2021
Published: March 9, 2021

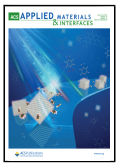

ACS Publications

https://dx.doi.org/10.1021/acsami.0c16866

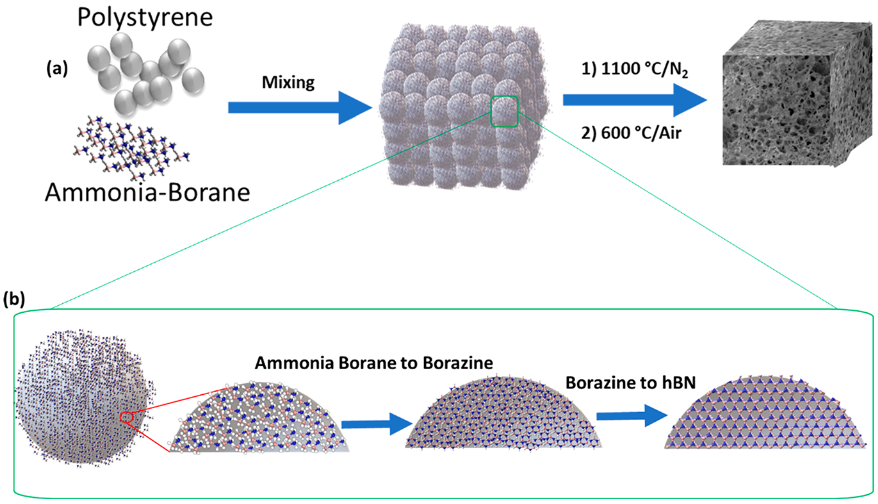

Figure 1. (a) Schematic of hBN aerogel synthesis, and (b) the reaction mechanism of hBN synthesis using ammonia borane as an hBN source.

Although graphene is not an appropriate choice for high-temperature applications in air, the basic concepts obtained from the processing and design principles of graphene can be applied to other 2D materials, such as MXenes, molybdenum disulfide, and boron nitride, for the development of aerogels with unexpected functionalities.[22,23] Among these 2D-nanostructures, hexagonal boron nitride (hBN) has attracted significant interest because of its electrical insulation and outstanding thermal and chemical stability.[17,24,25]

Over the past few years, various lightweight hBN-based aerogels and their polymer composites have successfully been fabricated by CVD, chemical functionalization, template, and sintering methods.[17,19,26−28] These synthesis methods of hBN aerogels have generally resulted in compounds of random hBN phases and a distribution of pore size and geometry. However, processing challenges, such as controlling interfacial interactions, maintaining dispersion, or other viscosity-related issues, can lead to poor load transfer, weak cross-linking between nanosheets, and/or limited deformability of the characteristic templates, preventing their widespread use in many applications of interest.[32]

Here, we report the fabrication of ultralightweight and fire-resistant hBN-based aerogels using ammonia borane (AB) as a precursor and polystyrene (PS) nanoparticles as a template. The resulting ultralightweight hBN aerogels consist of interconnected spherical pores due to the use of PS nanoparticles as the template. Various polymers, which have different levels of interfacial interactions with hBN-sheets, are infiltrated into the fabricated hBN aerogel to create composite aerogels with tunable properties, such as density, mechanical, and thermal properties. We have performed spectroscopic and microscopic characterizations to reveal the structure and morphology of the hBN aerogels and polymer composite aerogels. Morphology, compressive mechanical behavior, mechanical damping, and thermal properties of the hBN-polymer composite aerogels are investigated. The rigid nature of hBN aerogels becomes more flexible after infiltration of poly(dimethylsiloxane) (PDMS) and the composite aerogel remain porous after polymer penetration. The hBN-PDMS composite aerogels are completely recoverable after 99% strain compression in ∼1 h. We show that the hBN-polymer aerogels have high energy dissipation associated with their mechanical damping behavior and thermal conductivity of the composite aerogels can be tuned from insulator to conductive by polymer infiltration. Finally, to understand the role of interfacial interactions on the mechanical behavior of the hBN-polymer structure, density functional theory (DFT) calculations have been performed.

RESULTS AND DISCUSSIONS

hBN aerogels are fabricated using solid AB as the precursor and PS nanoparticles as the template. Mixing AB and PS nanoparticles leads to the formation of a self-assembled hybrid nanocomposite, as shown in Figure 1. Key here is that the AB adsorbs atop the surface of PS nanoparticles due to intermolecular interactions between AB and PS nanoparticles. Subsequent high-temperature annealing of the hybrid nanocomposite resulted in the formation of an aerogel, as the AB was converted into hBN and the PS nanoparticles were removed via pyrolysis (Figure 1a). More specifically, the molecular AB that adsorbed atop the surface of PS nanoparticles decomposed into aminoborane at ∼100 °C. Borazine forms at ∼150 °C, which is the main building block for hBN synthesis.[29] It undergoes dehydrogenation and produces interconnected hBN sheets atop the surface of PS nanoparticles with increasing temperature to 1100 °C for 6 h under nitrogen (Figure 1b).[29] After complete removal of the PS nanoparticles by decomposition at 600 °C for 7 h under air, an ultralightweight hBN aerogel with interconnected spherical porous structures isobtained.

To reveal the structure and morphology of the hBN aerogels, spectroscopic and microscopic characterizations were performed. X-ray photoelectron spectroscopy (XPS) was used for quantitative chemical analysis (Figure S1). The N 1s core level peak position of the nitrogen atoms is at 399.1 eV and the peak position of the boron atom is ∼192.1 eV.[19] In addition, C and O atoms were detected at 285 and 533 eV, respectively, due to residues of PS nanoparticles and oxidation of hBN during the pyrolysis of PS nanoparticles (Figure S1a).[19] In high-resolution XPS, the peaks of the B 1s and N 1s for the B—N bonding appeared at the binding energies of 191.8 and 405.8 eV, respectively, which are in good agreement with the values reported in the literature (Figure S1b,c).[19] Raman spectroscopy was used to examine the bonding characteristics and phase purity of the hBN aerogel. It revealed the characteristic Raman scattering peak at 1365.1 cm^{-1} that

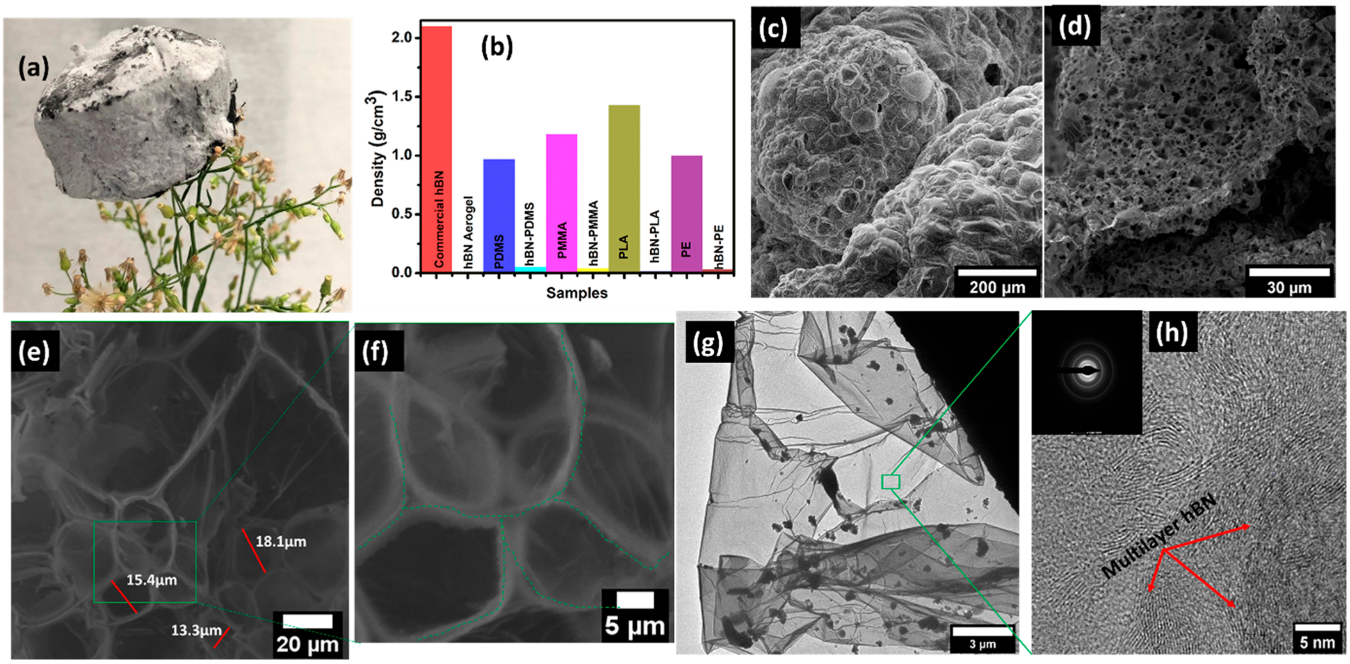

Figure 2. (a) Ultralightweight hBN aerogel, (b) density of hBN aerogel and various hBN-polymer composite aerogels with infiltrated polymers, (c) SEM image of hBN-PS structure before burning out PS colloidal nanoparticles, (d−f) SEM images of hBN aerogels showing interconnected spherical porous morphology, and (g,h) low- and high-resolution TEM images of hBN aerogels showing large polycrystalline structure of hBN, respectively.

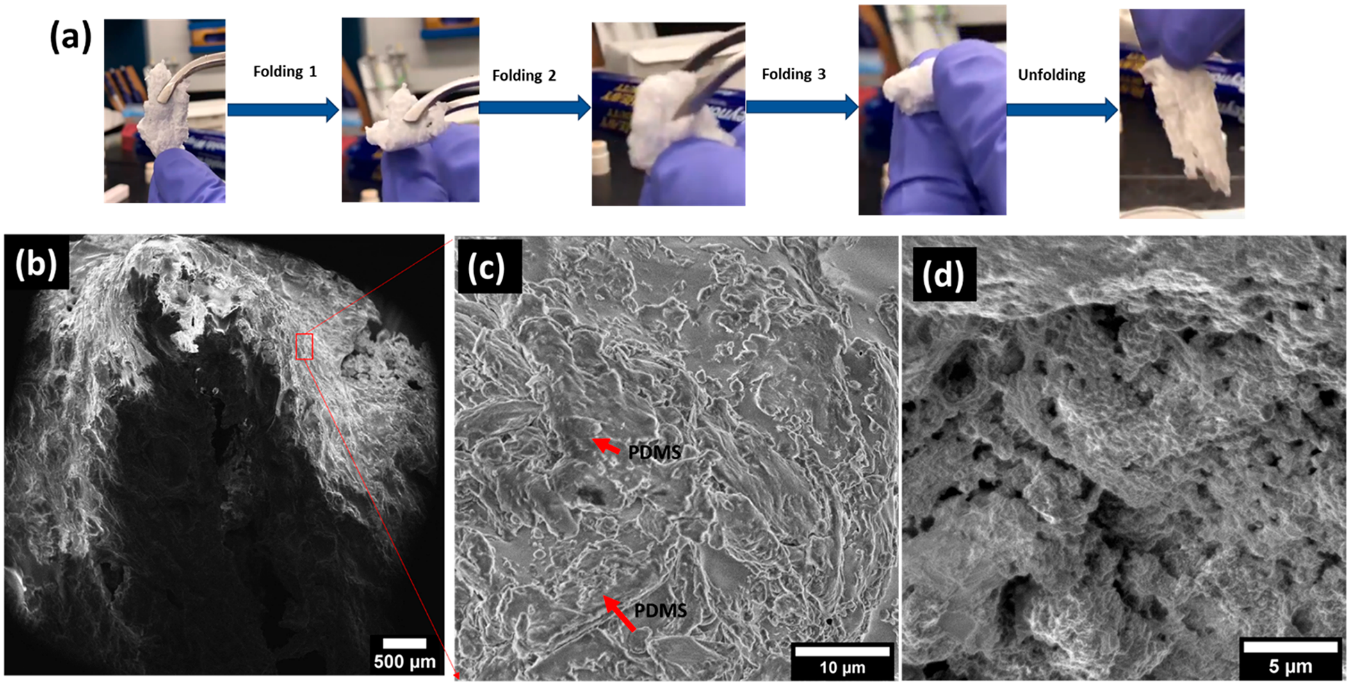

Figure 3. (a) Optical images of flexible and foldable hBN-PDMS composite aerogel, SEM images of (b) ~180° bended hBN-PDMS aerogel, (c) the surface of hBN-PDMS aerogel, and (d) porous structure of hBN-PDMS aerogel.

corresponds to the in-plane E_{2g} phonon mode of hBN (Figure S2a).[30] In addition to the spectroscopic characterizations, scanning electron microscopy (SEM) and transmission electron microscopy (TEM) were used to examine the aerogel structure. To identify chemical functional groups on the hBN structure, Fourier-transform infrared (FTIR) characterization was performed (Figure S2b). Besides the characteristic peaks of B—N, the spectrum of the hBN aerogel contained peaks corresponding to B—N—O at 940 cm^{-1}. The peak at 1167 cm^{-1} corresponds to the B—O—H and C—BN in-plane bending. The presence of an additional functional group at ~1690 cm^{-1} corresponds to BN—C═O and the broad peak at ~3300 cm^{-1} correspond to −OH functional groups.

The resulting hBN aerogel is ultralightweight with the density of 0.0064 g/cm^3 compared to commercially exfoliated hBN structures (2.1 g/cm^3) (Figure 2a). The composite

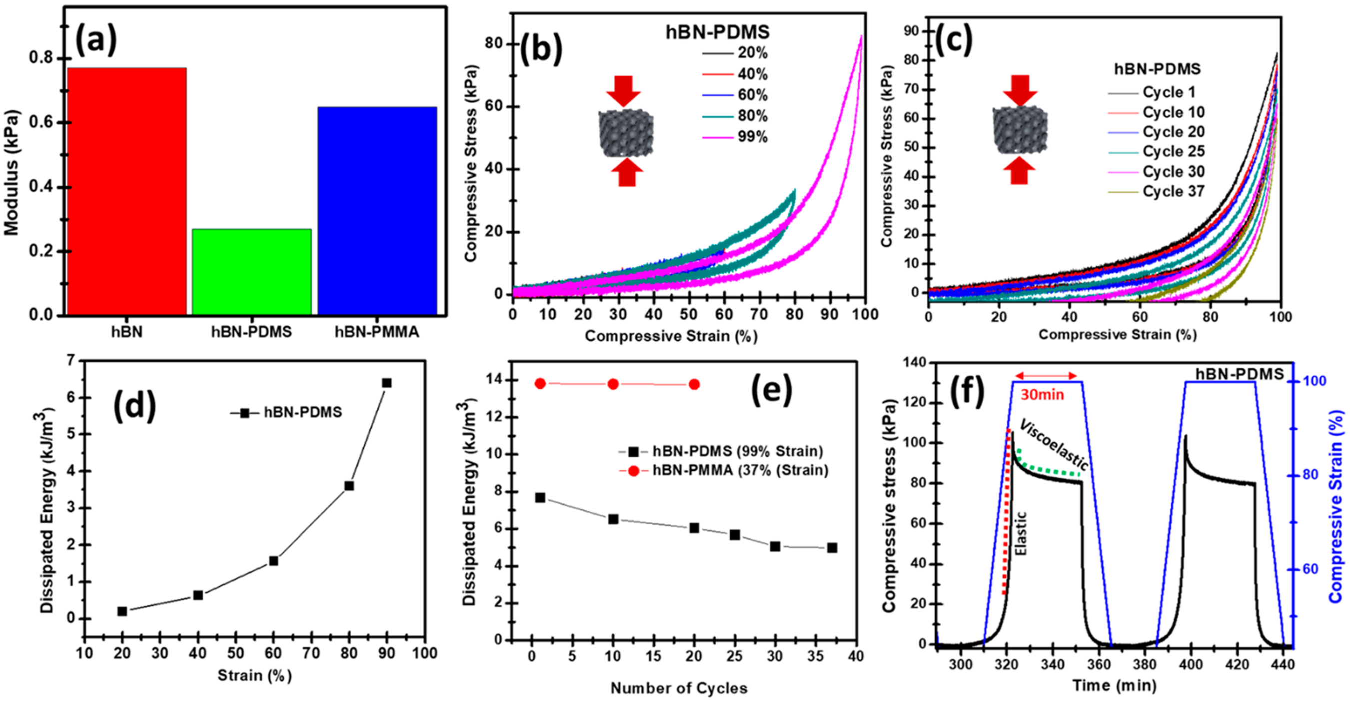

Figure 4. (a) Young's modulus of hBN and hBN composite aerogels, (b) compression load−unload of hBN-PDMS composite aerogel from 20% to 99% strain, (c) cyclic compression of hBN-PDMS aerogel. (d,e) Energy dissipation of hBN-polymer composite aerogels using PDMS and PMMA, and (f) stress-relaxation test of hBN-PDMS composite aerogels.

aerogels were prepared by infiltrating with various additives. The infiltration process was performed using PDMS, poly(methyl methacrylate) (PMMA), polylactic acid (PLA), and polyethylene (PE) in toluene at atmospheric pressure and room temperature for 24 h. The density of the hBN composite aerogels with these additives is shown in Figure 2b. The densities of the hBN composites aerogels decrease to 0.0521, 0.0426, 0.0171, 0.0331 g/cm^3 after infiltration with PDMS, PMMA, PLA, and PE, respectively. For reference, the densities of PDMS, PMMA, PLA, and PE are 0.97, 1.18, 1.43, and 1 g/cm^3 (Figure 2b). In addition, the density of hBN-composite aerogels could be tailored by varying the additive solution concentration and infiltration time, as shown for hBN-PDMS composite aerogels (Figure S3).

SEM images in Figure 2c show the hBN-PS self-assembled composite prior to removal of PS nanoparticles. The structure of the hBN aerogel after PS removal is shown in Figure 2d. It consists of a highly porous cellular architecture with nearly spherical pores. The interconnected structure of circular and oval shaped pores with narrow distribution is presented in Figures 2e,f. The size of the interconnected pores was ∼20 times greater than the size of the PS nanoparticles, which is most probably due to aggregation of PS nanoparticles. TEM was used to gain insight into the morphology of the hBN structure. A representative low-magnification TEM image shows large folded hBN sheets with small hBN particles (Figure 2g). High-resolution TEM images also revealed the polycrystalline structure of hBN (Figure 2h). The darker regions and lines in Figure 2h show the hBN sheet with a few-layers structure. It also exhibits the smaller grain structure of the hBN sheet. In addition, a small proportion of amorphous hBN also has been observed in TEM characterization.

The properties of hBN aerogels can be tailored by infiltrating polymer additives for a desired application.[31,32] Here, we fabricated various hBN-polymer composite aerogels but discuss in detail those infiltrated with PDMS and PMMA. The morphologies of the hBN-polymer composite aerogels have also been investigated. Figure 3a shows a representative image of a PDMS-infiltrated hBN aerogel. As a result of PDMS infiltration, a flexible and foldable hBN composite aerogel was obtained that can be repeatedly bent and folded without destroying its original shape (Figure 3a,b). SEM images indicate that the hBN-PDMS composite aerogel remained nanoporous (Figure 3c,d).

Nitrogen adsorption−desorption isotherms and pore size distributions of the aerogels were measured at 77 K in powder form. The Brunauer−Emmett−Teller (BET) specific surface area was calculated from the nitrogen adsorption isotherms. The hBN and hBN-PDMS aerogels exhibit a high BET specific surface area of 895.8 and 518.4 m^2/g, respectively. The measured isotherm of hBN and hBN-PDMS aerogels illustrate a typical type IV isotherm, in which adsorption on the surface of solids proceeds via multilayer adsorption followed by capillary condensation.[35] The pore size distributions are calculated by the Barrett−Joyner−Halenda (BJH) method for hBN and hBN-PDMS aerogels (Figure S4b).

Figure 4 shows the compressive mechanical behavior of the hBN aerogel composites. The hBN aerogel has a compressive modulus of ∼0.77 kPa between 0 and 40% strain (ε). The modulus of the hBN aerogel decreased to 0.27 and 0.65 kPa after PDMS and PMMA penetration, respectively. The pure hBN aerogel exhibits a nonlinear and nonmonotonic behavior because of the highly porous and brittle nature of hBN. The hBN aerogel pores are partially collapsed between 48 and 56% strain and the aerogel fractured at 71.4% ε (Figure S5). The compressive stress−strain measurements of hBN-PDMS with gradually increasing strain from 20% to 99% are shown in Figure 4b. The compression stress−strain curves of hBN-

PDMS composite aerogel display the characteristic behavior of porous sponge-like materials with three distinct stages.[17] When the hBN–PDMS composite aerogel is compressed at $\varepsilon < 40\%$, the composite aerogel deformed linearly with respect to the stress. The region between 40% and 70% strain exhibited elastic buckling and densification of the structure. With the stress increasing at $\varepsilon > 70\%$, the hBN-PDMS composite aerogel structure was compacted and behaves like a bulk material because of the reduced porosity. When the force is released, the unloading curve returns to the origin without measurable plastic deformation. The maximum stress increased from 5.7 to 82.4 kPa with an increase in the strain from 20% to 99%, which indicates the hBN–PDMS composite aerogel could tolerate large deformation.

To understand the mechanical stability of the composite aerogels, we performed load–unload cycling measurements between zero and a maximum strain of 99% and 37% for hBN-PDMS and hBN-PMMA, respectively (Figures 4c and S6). For a small number of cycles (<20 cycles) in both cases, the material returns to its initial shape. However, as the number of mechanical cycles increases beyond 20, the material retains some compressive strain after completing the experiment. This strain is not permanent as the viscoelasticity allows the material to recover its full shape within an hour.

Both hBN-PDMS and hBN-PMMA composite aerogels show hysteresis during the compressive loading–unloading cycles, which indicates that hBN-polymer aerogels have significant mechanical damping properties. To quantify the damping capability of the composite aerogels, the estimated dissipated energy, which corresponds to the area of the hysteresis loop during compressive cycles at different strain, was calculated using eq 1 (Figure 4d,e)

$$\int \sigma \mathrm{d}\varepsilon \qquad (1)$$

where σ is the measured compressive stress and ε is the applied compressive strain. As shown in Figure 4d, extending the test to higher strains resulted in larger dissipative energy, which is defined as the energy dissipated per unit volume. In Figure 4e, the dissipative energy of the hBN-PDMS composite aerogels decreased over the first 30 cycles and then approached a constant. Conversely, the dissipative energy of the hBN-PMMA aerogel remained approximately constant over 20 compression cycles. The dissipation energy for the composite hBN-polymer aerogels indicates that the mechanical damping properties can be explained by interfacial sliding between hBN nanosheets and polymer chains. Compared to the 2D structure of hBN, the hBN-polymer composite material contains polymer chains attached to the surface of the hBN component. Thus, it would be expected that the composite material would have additional mechanisms for dissipation associated with interactions at the interfaces such as π–π, hydrophobic, and van der Waals among the hBN sheets and polymer chains. We hypothesize that when the composite was mechanically cycled at large enough strain, the polymer supported hBN-flakes can repeatedly buckled and recover. As a result, interfacial slippage promoted and frictional energy dissipated through the weakly interacting hBN and polymer chains and the noncovalent interface interactions. Hence the overall mechanical damping behavior of the composite aerogels can be greater than the pure hBN material.

Stress relaxation tests were performed to investigate the viscoelastic behavior of the composite aerogels by applying a constant strain and measuring the load required to maintain it as a function of time for 15 cycles (Figures 4f and S6). A 99.8% of the constant strain was applied on the hBN-PDMS composite aerogel, and the drop in stress as a function of time (30 min) was observed. The peak engineering stress decreased from 139.3 to ~105 kPa in the first three cycles then approaches being constant (Figure S7). Over time, the stress decay occurred at constant strain due to the viscoelasticity of the solid material (Figure 4f).

The mechanical damping behavior of the hBN-PDMS aerogels has been demonstrated qualitatively using a 5 mm steel ball (Figure S8). A steel ball was dropped from a particular height (H) onto a steel base, and the height (h) after rebound was measured. The ratio of heights ($(h \times 100)/H$) gives the resilience ratio. Resilience ratio is defined as the ratio of energy released in recovery from deformation to the energy required to produce the deformation. The steel ball was dropped onto a 10.2 mm thick steel block from 76 cm high, and the result was used as the control. While the resilience of the steel block was 22.4%, the resilience of the hBN-PDMS (9.5 mm thick) composite aerogel was 31.6%.

In order to understand the chemical nature of the significant recoverability exhibited by the hBN-PDMS aerogels, DFT optimization of an hBN-PDMS dimer system was carried out (Figure 5). The hydroxyl-terminated dimerized version of PDMS in the computational model was chosen. Although the experimental hBN was a porous material with polycrystalline structure separated by pores and grain boundaries, the hydrogen-passivated hBN ribbon in the computational model was chosen to be small enough for meaningful computational accuracy but large enough to allow for meaningful interfacial interactions with the PDMS dimer. This model assumed that the interaction between an hBN structure with a large surface area and a small polymer unit significantly contribute to the interfacial chemistry responsible for the observed macroscopic mechanical properties. The model provides a glimpse into

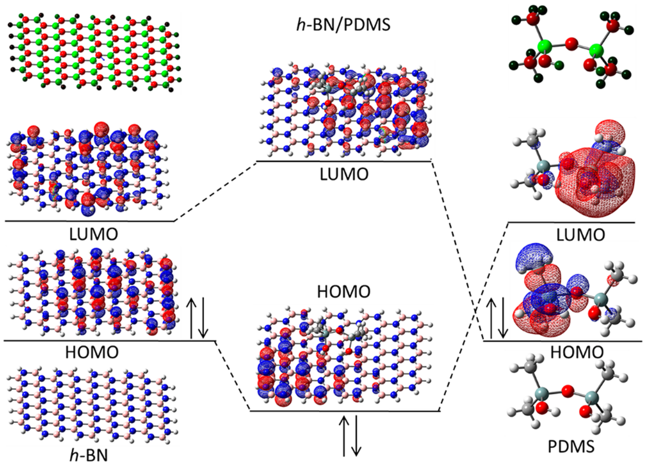

Figure 5. Frontier orbital mixing diagram between the hBN ribbon (left) and the PDMS dimer (right). Resulting frontier molecular orbitals for the hBN/PDMS system are shown in the middle. Besides the indicated HOMOs and LUMOs for the hBN ribbon and the PDMS dimer, charges around atoms are displayed in the top left and right corners. The greener the atom is, the closer to −1.326 Mulliken the atomic charge is; the redder the atom is, the closer to +1.326 Mulliken the atomic charge is.

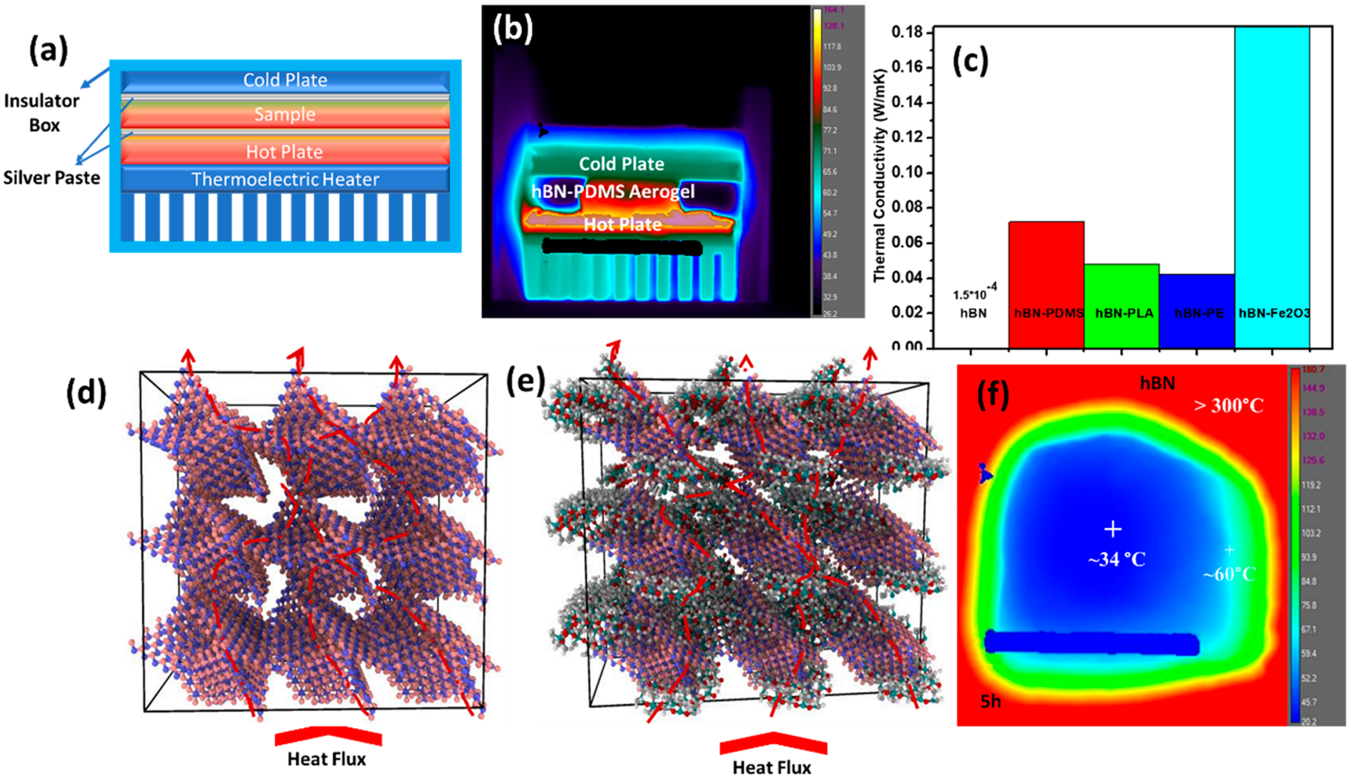

Figure 6. (a) Schematic representation of homemade thermal conductivity setup, (b) thermal conductivity setup for hBN-PDMS measurement, (c) thermal conductivity of hBN and hBN composite aerogels, (d,e) thermal conductivity mechanism of porous hBN composite and hBN-polymer composite aerogel, and (f) thermal camera images of insulation properties of hBN aerogel during 5 h at 300 °C.

some salient features that might play a significant role in the macroscopic properties observed experimentally.

The HOMO−LUMO gaps for the hBN ribbon (5.93 eV) and the PDMS dimer (7.75 eV) result in a lower HOMO−LUMO gap for the hBN-PDMS system (5.89 eV). The lower HOMO−LUMO gap indicates that the hBN-PDMS system was less stable than hBN or PDMS because of the noncovalent interface interaction between hBN and PDMS. The interaction energy (−0.27 eV) between hBN and PDMS confirmed a strong chemical affinity that was sufficient for a cohesion, but not strong enough to keep hBN and PDMS in a permanent structural arrangement. The optimized hBN-PDMS system revealed that the closest hBN-to-PDMS distance was 2.18 Å, which was between a nitrogen atom on the hBN ribbon and a hydrogen atom on the hydroxyl terminations. Hydrogen atoms on PDMS appeared to be closer to the hBN ribbon compared to carbon or silicon atoms of PDMS. Since the hydrogen atoms on the PDMS unit are the most positively charged atoms (see dark green atomic charges in top right illustration in Figure 5) and nitrogen atoms in the hBN unit were the most negatively charged atoms (see red−green atomic charges in top left illustration in Figure 5), a significant electrostatic attraction between PDMS hydrogen atoms and hBN nitrogen atoms occurred (see HOMO lobes in the hBN unit mostly around nitrogen atoms and HOMO lobes in the PDMS unit mostly around hydrogen atoms). These hydrogen-types of interactions were due to the strong electronegativity difference between hydrogen and nitrogen atoms, and these interactions were known to be highly reformable.[33] The chemical environment on the surface of the hBN thus allowed for a hydrogen-type of interfacial interaction to form, break, and reform more easily and faster than a covalent-type of interaction. The significant recoverability exhibited by the hBN-PDMS composite aerogel in compression (see Figure 4b,c) therefore is likely to be a direct consequence of the reformable character of the chemical affinity observed at the interface between both hBN and PDMS.

Thermal conductivity of hBN-polymer composite aerogels was measured to determine the effect of different polymer matrixes on the thermal conductivity of the hBN-polymer composite aerogels. The steady-state thermal conductivity was measured by a custom-built setup using a thermoelectric generator and infrared (IR) camera (Figure 6a,b). The pure hBN aerogels were thermally insulating. Figure 6c shows several examples displaying tunability of the thermal conductivity. The thermal conductivities of PDMS-, PLA-, PE- and Fe_2O_3-infiltrated hBN aerogels were 0.072, 0.048, 0.042, 0.19 W m^{-1} K^{-1}, respectively. Adding the appropriate additive increased the conductivity because of the high thermal resistance and interfacial phonon scattering existing between hBN and the additive matrix as well as their interfacial thermal resistance. Figure 6d represents the heat conduction pathway in the porous hBN aerogel. The highly porous architecture of hBN aerogels efficiently reduces the air conduction and convection and hence led to thermal conductivities below that of stationary air (Figure 6d). The thermal transport in porous solids is affected by the pore geometry, pore size, interconnection of the pores and wall thickness between pores. The thermal conductivity of the hBN-polymer aerogels was mainly determined by the heat capacitance of the polymer, the density of the thermal network, as well as the interfacial thermal resistance (Figure 6e). As shown in Figure 6f and Figure S10, the images from the infrared camera are represented with the color change from blue to red. This

https://dx.doi.org/10.1021/acsami.0c16866

shows that the hBN aerogels were completely insulating, while hBN-PDMS, hBN-PLA and hBN-Fe_2O_3 composite aerogels are thermally conductive. For reference, the thermal conductivity of PDMS, PLA, and Fe_2O_3 were 0.15, 0.193, and 0.595 W m^{-1} K^{-1}.

The thermal stabilities of hBN and hBN-PDMS composite aerogels were studied by thermogravimetric analysis (TGA) (Figure S11). The pure hBN aerogels lost ~7% of their weight which is consistent with an amorphous hBN structure. The hBN-PDMS composite aerogels decomposed in two steps which is related to amorphous hBN and PDMS. While amorphous hBN decomposed up to ~200 °C, the large amount of mass between ~200 and ~750 °C corresponds to PDMS loss.[33,34] At 800 °C, 31.3% of the weight still remained, which is attributed to the crystalline hBN structure. In addition, to illustrate the fire-resistant features of the pure hBN aerogel, we designed a propane flame torch (>1000 °C) experiment (see Video S1). The structure remained stable and unmodified after the flame exposure.

CONCLUSION

We report the fabrication of ultralightweight, flexible, foldable, and fire-resistant hBN and hBN-polymer composite aerogels with control over properties using AB as a precursor and PS nanoparticles as a template. We studied the compressive mechanical behavior of the hBN aerogels with different additives and reported that the properties of hBN-polymer composite aerogels could be tuned by the infiltration of different additives. The ultralightweight hBN aerogels consist of interconnected spherical pores due to the PS colloid template. By infiltration with PDMS, a highly viscoelastic aerogel composite can be obtained, which is completely recoverable after 99.8% strain compression. We showed that the hBN-polymer aerogels have a strong energy dissipation ability, which gives rise to their mechanical damping behavior. Thermal conductivity of the composite aerogels can be tuned from insulator to conductive by infiltration with the appropriate additive matrix. In addition to understanding the interfacial interactions between hBN and PDMS that results in the mechanical flexibility and recoverability of the hBN-PDMS aerogel, DFT calculations were performed. The DFT calculations revealed that the chemical affinity of the hBN and PDMS interface plays a key role on the mechanical properties of the composite aerogels.

EXPERIMENTAL SECTION

hBN based aerogels were fabricated using solid AB as a precursor and PS nanoparticles as a template. More specifically, 0.2 g of PS nanoparticles and 1 g of AB were mixed in solid phase. The AB-PS mixture was annealed at 1100 °C in CVD for 6 h under nitrogen, then the PS colloids were removed by decomposition at 600 °C for 7 h under air atmosphere. The composite aerogels were prepared by infiltrating additives. The infiltration process was performed using PDMS, PMMA, PLA, PE, and Fe_2O_3 in toluene at atmospheric pressure and room temperature for 24 h. The concentration of PDMS was 0.1 mg/mL in toluene and other additive concentrations were 5 mg/mL. More specifically, the liquid-state PDMS and cross-linker (Sylgard 184) was diluted in toluene and infiltrated into the pores within the hBN aerogel. After the PDMS infiltration, the composite was left in an oven at 100 °C for 2 h to cure the PDMS.

All aerogel samples were analyzed by SEM (FEI Quanta 200 FEG ESEM) and transmission electron microscopy (Talos F200X scanning/transmission electron microscope (S/TEM)). X-ray diffraction characterization was analyzed using the Bruker D8 Discover X-ray diffractometer. Raman spectroscopy analysis was collected using a Horiba Raman spectrometer with a 532 nm wavelength laser. XPS characterization was carried out using Thermo Fisher K-Alpha + X-ray photoelectron spectrometer (XPS/UPS). Thermo Fisher Scientific Nicolet iS50 Fourier transform infrared (FTIR) spectrometer was used for analyzing functional group of aerogels. Mechanical compression test was done by Instron 5969 with the rate of 0.1 mm/min at room temperature. The cyclic stress−relaxation test was conducted at 99.8% constant strain with the 30 min relaxation time for 15 cycles.

ASSOCIATED CONTENT

Supporting Information

The Supporting Information is available free of charge at https://pubs.acs.org/doi/10.1021/acsami.0c16866.

> XPS, Raman, and FTIR, spectra of hBN and hBN-PDMS composite aerogels, the N_2 absorption isotherms of hBN and hBN-PDMS aerogels, compressive stress−strain curve of hBN, hBN-PMMA composite aerogels, stress relaxation spectra of hBN-PDMS and hBN-PMMA composite aerogels, the damping behavior of hBN-PDMS composite aerogel, thermal conductivity of measurement setup with hBN, hBN-PDMS, hBN-PE, and hBN-PLA composite aerogels, thermogravimetric analysis of hBN and hBN-PDMS composite aerogels, morphology of PS nanoparticles (PDF)
>
> Fire resistant behavior of hBN aerogels (MP4)

AUTHOR INFORMATION

Corresponding Authors

Craig B. Arnold − *Princeton Institute for the Science and Technology of Materials and Department of Mechanical and Aerospace Engineering, Princeton University, Princeton, New Jersey 08540, United States;* orcid.org/0000-0002-0293-5411; Email: cbarnold@princeton.edu

Rodney D. Priestley − *Princeton Institute for the Science and Technology of Materials and Chemical and Biological Engineering, Princeton University, Princeton, New Jersey 08540, United States;* orcid.org/0000-0001-6765-2933; Email: rpriestl@princeton.edu

Authors

Sehmus Ozden − *Princeton Institute for the Science and Technology of Materials, Chemical and Biological Engineering, and Department of Mechanical and Aerospace Engineering, Princeton University, Princeton, New Jersey 08540, United States;* orcid.org/0000-0002-8073-1633

Nikita S. Dutta − *Princeton Institute for the Science and Technology of Materials and Department of Mechanical and Aerospace Engineering, Princeton University, Princeton, New Jersey 08540, United States;* orcid.org/0000-0003-2301-4010

Katelyn Randazzo − *Chemical and Biological Engineering, Princeton University, Princeton, New Jersey 08540, United States*

Thierry Tsafack − *Department of Materials Science and Nanoengineering, Rice University, Houston, Texas 77005, United States*

Complete contact information is available at: https://pubs.acs.org/10.1021/acsami.0c16866

Author Contributions

S.O., C.B.A., and R.D.P originated the project ideas and S.O. performed the fabrication. N.S.D. conducted TEM characterization. K.R. synthesized PS nanoparticles. T.T. performed DFT calculations. S.O., C.B.A., and R.D.P. wrote the manuscript. All of the authors discussed the results and commented on the manuscript.

Notes

The authors declare no competing financial interest.

■ ACKNOWLEDGMENTS

S.O. acknowledges financial support from the Princeton Center for Complex Materials (PCCM) Postdoctoral Fellowship. The authors acknowledge the use of Princeton's Imaging and Analysis Center, which is partially supported through the Princeton Center for Complex Materials (PCCM), a National Science Foundation (NSF)-MRSEC program (DMR-2011750).

■ REFERENCES

(1) Gesser, H. D.; Goswami, P. C. Aerogels and Related Porous Materials. *Chem. Rev.* **1989**, *89* (4), 765−788.

(2) Koebel, M.; Rigacci, A.; Achard, P. Aerogel-Based Thermal Superinsulation: An Overview. *J. Sol-Gel Sci. Technol.* **2012**, *63* (3), 315−339.

(3) Biener, J.; Stadermann, M.; Suss, M.; Worsley, M. a.; Biener, M. M.; Rose, K. a.; Baumann, T. F. Advanced Carbon Aerogels for Energy Applications. *Energy Environ. Sci.* **2011**, *4* (3), 656−667.

(4) Randall, J. P.; Meador, M. A. B.; Jana, S. C. Tailoring Mechanical Properties of Aerogels for Aerospace Applications. *ACS Appl. Mater. Interfaces* **2011**, *3* (3), 613−626.

(5) Pierre, A. C.; Pajonk, G. M. Chemistry of Aerogels and Their Applications. *Chem. Rev.* **2002**, *102* (11), 4243−4265.

(6) Montes, S.; Maleki, H. *Aerogels and Their Applications*; Elsevier Inc., 2020; pp 337−399.

(7) Baetens, R.; Jelle, B. P.; Gustavsen, A. Aerogel Insulation for Building Applications: A State-of-the-Art Review. *Energy Build.* **2011**, *43* (4), 761−769.

(8) Bheekhun, N.; Rahim, A.; Talib, A.; Hassan, M. R. Aerogels in Aerospace: An Overview. *Adv. Mater. Sci. Eng.* **2013**, *2013* (65), 1−18.

(9) Ozden, S.; Tiwary, C. S.; Hart, A. H. C.; Chipara, A. C.; Romero-Aburto, R.; Rodrigues, M.-T. F.; Taha-Tijerina, J.; Vajtai, R.; Ajayan, P. M. Density Variant Carbon Nanotube Interconnected Solids. *Adv. Mater.* **2015**, *27* (11), 1842−1850.

(10) Rechberger, F.; Niederberger, M. Synthesis of Aerogels: From Molecular Routes to 3-Dimensional Nanoparticle Assembly. *Nanoscale Horizons* **2017**, *2* (1), 6−30.

(11) Vinod, S.; Tiwary, C. S.; da Silva Autreto, P. A.; Taha-Tijerina, J.; Ozden, S.; Chipara, A. C.; Vajtai, R.; Galvao, D. S.; Narayanan, T. N.; Ajayan, P. M. Low-Density Three-Dimensional Foam Using Self-Reinforced Hybrid Two-Dimensional Atomic Layers. *Nat. Commun.* **2014**, *5* (1), 1−9.

(12) Zu, G.; Shen, J.; Zou, L.; Wang, W.; Lian, Y.; Zhang, Z.; Du, A. Nanoengineering Super Heat-Resistant, Strong Alumina Aerogels. *Chem. Mater.* **2013**, *25* (23), 4757−4764.

(13) Du, A.; Zhou, B.; Shen, J.; Xiao, S.; Zhang, Z.; Liu, C.; Zhang, M. Monolithic Copper Oxide Aerogel via Dispersed Inorganic Sol-Gel Method. *J. Non-Cryst. Solids* **2009**, *355* (3), 175−181.

(14) Du, A.; Zhou, B.; Shen, J.; Gui, J.; Zhong, Y.; Liu, C.; Zhang, Z.; Wu, G. A Versatile Sol-Gel Route to Monolithic Oxidic Gels via Polyacrylic Acid Template. *New J. Chem.* **2011**, *35* (5), 1096−1102.

(15) Meador, M. A. B.; Alemán, C. R.; Hanson, K.; Ramirez, N.; Vivod, S. L.; Wilmoth, N.; McCorkle, L. Polyimide Aerogels with Amide Cross-Links: A Low Cost Alternative for Mechanically Strong Polymer Aerogels. *ACS Appl. Mater. Interfaces* **2015**, *7* (2), 1240−1249.

(16) Du, R.; Hu, Y.; Hübner, R.; Joswig, J. O.; Fan, X.; Schneider, K.; Eychmüller, A. Specific Ion Effects Directed Noble Metal Aerogels: Versatile Manipulation for Electrocatalysis and Beyond. *Sci. Adv.* **2019**, *5* (5), eaaw4590.

(17) Xu, X.; Zhang, Q.; Hao, M.; Hu, Y.; Lin, Z.; Peng, L.; Wang, T.; Ren, X.; Wang, C.; Zhao, Z.; Wan, C.; Fei, H.; Wang, L.; Zhu, J.; Sun, H.; Chen, W.; Du, T.; Deng, B.; Cheng, G. J.; Shakir, I.; Dames, C.; Fisher, T. S.; Zhang, X.; Li, H.; Huang, Y.; Duan, X. Double-Negative-Index Ceramic Aerogels for Thermal Superinsulation. *Science* **2019**, *363* (6428), 723−727.

(18) Yousefi, N.; Lu, X.; Elimelech, M.; Tufenkji, N. Environmental Performance of Graphene-Based 3D Macrostructures. *Nat. Nanotechnol.* **2019**, *14* (2), 107−119.

(19) Sudeep, P. M.; Vinod, S.; Ozden, S.; Sruthi, R.; Kukovecz, A.; Konya, Z.; Vajtai, R.; Anantharaman, M. R.; Ajayan, P. M.; Narayanan, T. N. Functionalized Boron Nitride Porous Solids. *RSC Adv.* **2015**, *5* (114), 93964−93968.

(20) Bian, R.; He, G.; Zhi, W.; Xiang, S.; Wang, T.; Cai, D. Ultralight MXene-Based Aerogels with High Electromagnetic Interference Shielding Performance. *J. Mater. Chem. C* **2019**, *7* (3), 474−478.

(21) Wu, Y. P.; Yi, N. B.; Huang, L.; Zhang, T. F.; Fang, S. L.; Chang, H. C.; Li, N.; Oh, J. Y.; Lee, J. A.; Kozlov, M.; Chipara, A. C.; Terrones, H.; Xiao, P. S.; Long, G. K.; Huang, Y.; Zhang, F.; Zhang, L.; Lepró, X.; Haines, C.; Lima, M. D.; Lopez, N. P.; Rajukumar, L. P.; Elias, A. L.; Feng, S. M.; Kim, S. J.; Narayanan, N. T.; Ajayan, P. M.; Terrones, M.; Aliev, A.; Chu, P. F.; Zhang, Z.; Baughman, R. H.; Chen, Y. S. Three-Dimensionally Bonded Spongy Graphene Material with Super Compressive Elasticity and Near-Zero Poisson's Ratio. *Nat. Commun.* **2015**, *6* (6), 6141−6150.

(22) Shi, S.; Qian, B.; Wu, X.; Sun, H.; Wang, H.; Zhang, H.; Bin; Yu, Z. Z.; Russell, T. P. Self-Assembly of MXene-Surfactants at Liquid−Liquid Interfaces: From Structured Liquids to 3D Aerogels. *Angew. Chem., Int. Ed.* **2019**, *58* (50), 18171−18176.

(23) Shen, J.; Zhu, Y.; Jiang, H.; Li, C. 2D Nanosheets-Based Novel Architectures: Synthesis, Assembly and Applications. *Nano Today* **2016**, *11* (4), 483−520.

(24) Li, G.; Zhu, M.; Gong, W.; Du, R.; Eychmüller, A.; Li, T.; Lv, W.; Zhang, X. Boron Nitride Aerogels with Super-Flexibility Ranging from Liquid Nitrogen Temperature to 1000 °C. *Adv. Funct. Mater.* **2019**, *29* (20), 1900188.

(25) Yin, J.; Li, X.; Zhou, J.; Guo, W. Ultralight Three-Dimensional Boron Nitride Foam with Ultralow Permittivity and Superelasticity. *Nano Lett.* **2013**, *13* (7), 3232−3236.

(26) Owuor, P.; Park, O.-K.; Woellner, C.; Jalilov, A.; Susarla, S.; Joyner, J.; Ozden, S.; Duy, L.; Villegas Salvatierra, R.; Vajtai, R.; Tour, J.; Lou, J.; Galvao, D.; Tiwary, C.; Ajayan, P. Lightweight Hexagonal Boron Nitride Foam for CO_2 Absorption. *ACS Nano* **2017**, *11* (9), 8944−8952.

(27) Zeng, X.; Ye, L.; Yu, S.; Sun, R.; Xu, J.; Wong, C. P. Facile Preparation of Superelastic and Ultralow Dielectric Boron Nitride Nanosheet Aerogels via Freeze-Casting Process. *Chem. Mater.* **2015**, *27* (17), 5849−5855.

(28) Gautam, C.; Chakravarty, D.; Gautam, A.; Tiwary, C.; Woellner, C.; Mishra, V.; Ahamad, N.; Ozden, S.; Jose, S.; Biradar, S.; Vajtai, R.; Trivedi, R.; Galvao, D.; Ajayan, P. Synthesis and 3D Interconnected Nanostructured H-BN-Based Biocomposites by Low-Temperature Plasma Sintering: Bone Regeneration Applications. *ACS Omega* **2018**, *3* (6), 6013−6021.

(29) Frueh, S.; Kellett, R.; Mallery, C.; Molter, T.; Willis, W. S.; King'Ondu, C.; Suib, S. L. Pyrolytic Decomposition of Ammonia Borane to Boron Nitride. *Inorg. Chem.* **2011**, *50* (3), 783−792.

(30) Lei, W.; Mochalin, V. N.; Liu, D.; Qin, S.; Gogotsi, Y.; Chen, Y. Boron Nitride Colloidal Solutions, Ultralight Aerogels and Free-standing Membranes Through One-Step Exfoliation and Functionalization. *Nat. Commun.* **2015**, *6* (1), 1−8.

(31) Guan, L. Z.; Zhao, L.; Wan, Y. J.; Tang, L. C. Three-Dimensional Graphene-Based Polymer Nanocomposites: Preparation, Properties and Applications. *Nanoscale* **2018**, *10* (31), 14788−14811.

(32) Kinloch, I. A.; Suhr, J.; Lou, J.; Young, R. J.; Ajayan, P. M. Composites with Carbon Nanotubes and Graphene: An Outlook. *Science* **2018**, *362* (362), 547−553.

(33) Chipara, A.C.; Tsafack, T.; Owuor, P.S.; Yeon, J.; Junkermeier, C.E.; van Duin, A.C.T.; Bhowmick, S.; Asif, S.A.S.; Radhakrishnan, S.; Park, J.H.; Brunetto, G.; Kaipparettu, B.A.; Galvao, D.S.; Chipara, M.; Lou, J.; Tsang, H.H.; Dubey, M.; Vajtai, R.; Tiwary, C.S.; Ajayan, P.M. Underwater Adhesive Using Solid Liquid Polymer Mixes. *Materials Today Chemistry* **2018**, *9* (9), 149−157.

(34) Owuor, P. S.; Chaudhary, V.; Woellner, C. F.; Sharma, V.; Ramanujan, R. V.; Stender, A. S.; Soto, M.; Ozden, S.; Barrera, E. V.; Vajtai, R.; Galvão, D. S.; Lou, J.; Tiwary, C. S.; Ajayan, P. M. High Stiffness Polymer Composite with Tunable Transparency. *Mater. Today* **2018**, *21* (5), 475−482.

(35) Bardestani, R.; Patience, G. S.; Kaliaguine, S. Experimental Methods in Chemical Engineering: Specific Surface Area and Pore Size Distribution Measurements—BET,BJH, and DFT. *Can. J. Chem. Eng.* **2019**, *97* (11), 2781−2791.